PERGAMON

International Journal of Heat and Mass Transfer 45 (2002) 2011–2020

International Journal of HEAT and MASS TRANSFER

www.elsevier.com/locate/ijhmt

Heat transfer in a dimpled channel: combined influences of aspect ratio, temperature ratio, Reynolds number, and flow structure

G.I. Mahmood, P.M. Ligrani *

Department of Mechanical Engineering, Convective Heat Transfer Laboratory, University of Utah, 50 S. Central Campus Drive, Salt Lake City, UT 84112-9208, USA

Received 17 April 2001; received in revised form 2 October 2001

Abstract

Experimental results, measured on and above a dimpled test surface placed on one wall of a channel, are given for Reynolds numbers from about 600 to about 11 000 and ratios of air inlet stagnation temperature to surface temperature ranging from 0.78 to 0.94. These include flow visualizations, and spatially resolved local Nusselt numbers. Ratios of channel height to dimple print diameter of 0.20, 0.25, 0.50, and 1.00 are employed. The ratio of dimple depth to dimple print diameter is 0.2. Visualized flow smoke patterns show that the vortex pairs, which are periodically shed from the dimples, becomes stronger as non-dimensional channel height H/D decreases. Such behavior is leads to local Nusselt number augmentations at these same locations, which also become larger as H/D decreases. Local Nusselt number ratios also increase substantially at same locations as T_{oi}/T_w decreases because of buoyancy and variable property influences.

1. Introduction

Improvements in heat transfer augmentation levels in internal passages are useful in a variety of practical applications, including combustion chamber liners, and passages for internal cooling of turbine airfoils in gas turbine engines. One innovative technique, which is the subject of a number of recent investigations, involves the placement of dimples on surfaces of channels. According to Mahmood et al. [1], the use of such dimples produces augmented surface heat transfer levels (compared to channels with all smooth surfaces) because of: (i) the reattachment of the shear layer which forms across the top of each dimple, and (ii) the vortex structures and vortical fluid shed from each individual dimple indentation which then advect over the flat surface just downstream. In contrast, pressure drops and friction factors are usually not increased appreciably (compared to a channel with all smooth surfaces) because no form drag is produced by objects protruding into the flow [1].

A number of heat transfer studies from Russia utilize dimples. These studies employ flows over flat walls with regular arrays of spherical pits [2], flows in annular passages with a staggered array of concave dimples on the interior cylindrical surface [3], flows in single hemispherical cavities [4,5], flows in diffuser and convergent channels each with a single hemispherical cavity [6], and flows in a narrow channel with spherical shaped dimples placed in relative positions on two opposite surfaces [7]. Heat transfer augmentations as high as 150% compared to smooth surfaces, are reported sometimes with appreciable pressure losses [3].

More recently, Chyu et al. [8] presented data on the influences of Reynolds number on local heat transfer coefficient distributions on surfaces imprinted with staggered arrays of two different shapes of concavities. In some cases, enhancement of the overall heat transfer rate is about 2.5 times smooth surface values over a range of Reynolds numbers, and pressure losses are about half the values produced by conventional rib turbulators. Lin et al. [9] present computational

* Corresponding author. Tel.: +1-801-581-4240; fax: +1-801-585-9826.

E-mail address: ligrani@mech.utah.edu (P.M. Ligrani).

0017-9310/02/$ - see front matter
PII: S0017-9310(01)00314-3

Nomenclature

D	dimple print diameter
D_H	channel hydraulic diameter
H	channel height
h	heat transfer coefficient based on total surface area (dimples and flat), $q''/(T_w - T_m)$
k	thermal conductivity
Nu	Nusselt number, hD_H/k
Nu_0	baseline Nusselt number in a channel with smooth surfaces and no dimples
q''	surface heat flux
Re_H	Reynolds number based on channel height, $H\bar{U}/v$
t	time
t^*	normalized time $t\bar{U}/H$
T	temperature
$\bar{U}$	streamwise bulk velocity averaged over the channel cross-section
X	axial coordinate measured from test section inlet
Y	normal coordinate measured from test section dimple horizon
Z	spanwise coordinate measured from test section center-line

Greek symbol

v	kinematic viscosity

Subscripts

i	time-averaged, test section inlet value
m	time-averaged, local mixed-mean value
o	total or stagnation value
w	local wall value

simulation results of the flow structures, flow streamlines, temperature distributions, and resulting surface heat transfer distributions for the same geometries and flow conditions. Moon et al. [10] give data that illustrate the effects of channel height on heat transfer and pressure losses on a surface with a staggered pattern of dimples. According to the investigators, improvements in heat transfer intensification and pressure losses remain at approximately constant levels over the ranges of Reynolds number and channel height investigated. Mahmood et al. [1] describe the mechanisms responsible for local and spatially averaged heat transfer augmentations on flat channel surfaces with an array of dimples on one wall. Only one channel height, equal to 50% of the dimple print diameter, is used in the investigation.

The present study addresses the influences of dimples on flow structure and heat transfer. The investigation is different from other studies because:

(i) time-sequences of flow visualization images, illustrating instantaneous flow structure, are presented for different channel aspect ratios (and different ratios of channel height to dimple print diameter),

(ii) new spatially resolved Nusselt number data, showing the influences of buoyancy and variable properties (due to different inlet air-to-local wall temperature ratios), are given for different channel aspect ratios, and

(iii) all of these flow characteristics are discussed as they inter-relate to each other.

The magnitudes of non-dimensional parameters employed are the same as ones which exist in the internal cooling passages of the airfoils employed in gas turbines used for utility power generation. Particular attention is paid to alterations of flow structure and thermal characteristics with channel aspect ratio because of dramatic changes which occur as this parameter is varied, and because this allows some understanding of the influences of dimples in a variety of channel geometries.

2. Experimental apparatus and procedures

2.1. Channel and test surface for heat transfer measurements

A schematic of the facility used for heat transfer measurements is shown in Fig. 1(a). The air used within the facility is circulated in a closed-loop. One of two circuits is employed, depending upon the Reynolds number and flow rate requirements in the test section. For Reynolds numbers Re_H less than 20 000, a 102 mm pipe is connected to the intake of an ILG Industries 10P type centrifugal blower. For higher Reynolds numbers, a 203 mm pipe is employed with a New York Blower 7.5 HP, size 1808 pressure blower. In each case, the air mass flow rate from the test section is measured (upstream of which ever blower is employed) using an ASME standard orifice plate and Validyne M10 digital pressure manometer. The blower then exists into a series of two plenums (0.9 m^2 and 0.75 m^2). A Bonneville cross-flow heat exchanger is located between two of these plenums, and is cooled with liquid nitrogen at flow rate appropriate to give the desired air temperature at the exit of the heat exchanger. As the air exits the heat exchange, it enters the second plenum, from which the air passes into a rectangular bell mouth inlet, followed by a honeycomb, two screens, and two-dimensional 19.5 to 1 contraction ratio nozzle. This nozzles leads to a rectangular cross-section, 411 mm × 25.4 mm inlet duct which is

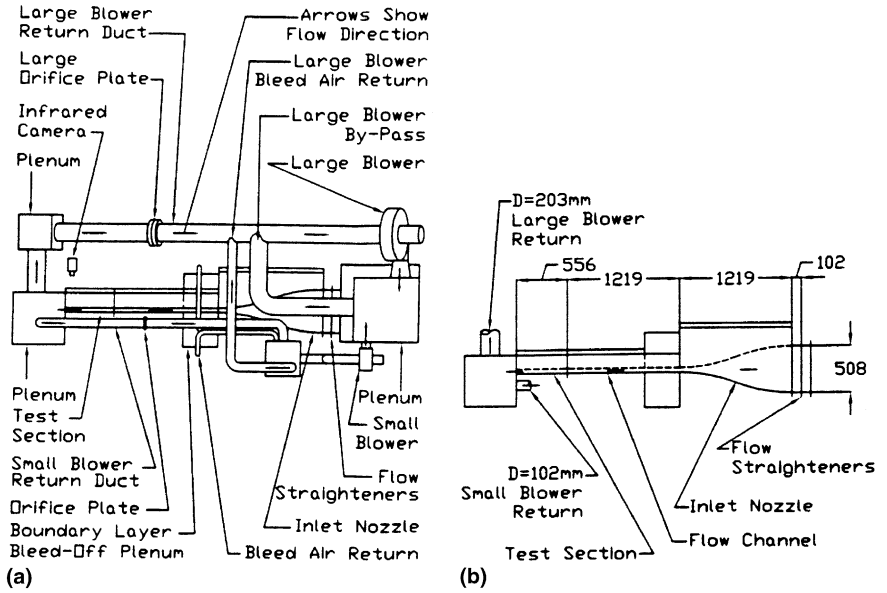

Fig. 1. Schematic diagrams of: (a) the experimental apparatus used for heat transfer measurements; (b) the experimental apparatus used for flow visualizations and measurement of flow structure. All dimensions are given in mm.

1219 mm in length. This is equivalent to 25.4 hydraulic diameters (where hydraulic diameter is 47.8 mm). A trip is employed on the bottom surface of the inlet duct, just upstream of the test section, which follows with the same cross-section dimensions. It exists to a 0.60 m square plenum, which is followed by two pipes, each containing an orifice plate, mentioned earlier.

Figs. 2(a) and (b) present the geometric details of the test surface, including dimple geometry. A total of 13 rows of dimples are employed in the streamwise direction, and nine rows are employed in the spanwise direction in a staggered array. Also identified in Fig. 2(a) is the test section coordinate system employed for the study. Note that the Y coordinate is normal from the test surface.

All exterior surfaces of the facility (between the heat exchanger and test section) are insulated with Styrofoam ($k = 0.024$ W/m K) or 2–3 layers of 2.54 cm thick, Elastomer Products black neoprene foam insulation ($k = 0.038$ W/m K) to minimize heat losses. Calibrated copper–constantan thermocouples are located between the three layers of insulation located beneath the test section to determine conduction losses. Between the first layer and the 3.2 mm thick acrylic, dimpled test surface is custom-made Electrofilm etched-foil heater (encapsulated between two thin layers of Kapton) to provide a constant heat flux boundary condition on the test surface. The acrylic surface contains 24 copper–constantan thermocouples, and is adjacent to the air stream. Each of these thermocouples is located 0.0508 cm just below this surface to provide measurements of local surface temperatures, after correction for thermal contact resistance and temperature drop through the 0.0508 cm thickness of acrylic. Acrylic is chosen because of its low thermal conductivity ($k = 0.16$ W/m K at 20 °C) to minimize and spanwise conduction along the test surface, and thus minimize "smearing" of spatially varying temperature gradients along the test surface. The surface of the acrylic is painted flat black to improve its surface emissivity for the infrared imaging. The power to the foil heater is controlled and regulated using a variac power supply. Energy balances, performed on the heated test surface, then allow determination of local magnitudes of the convective heat flux.

The mixed-mean temperature of the air entering the test section is measured using five calibrated copper–constantan thermocouples spread across its cross-section. Five calibrated copper–constantan thermocouples are also spread over the exit of the test section duct. Mixed-mean temperatures, estimated from measured temperatures, match values determined from energy balances within a few percent for all experimental conditions investigated. All measurements are obtained when the test facility at steady-state, achieved when each of the temperatures from the 24 thermocouples (on the test surface) vary by less than 0.1 °C over a 10 min period.

2.2. Local Nusselt number measurement

To determine the surface heat flux (used to calculate heat transfer coefficients), the convective power

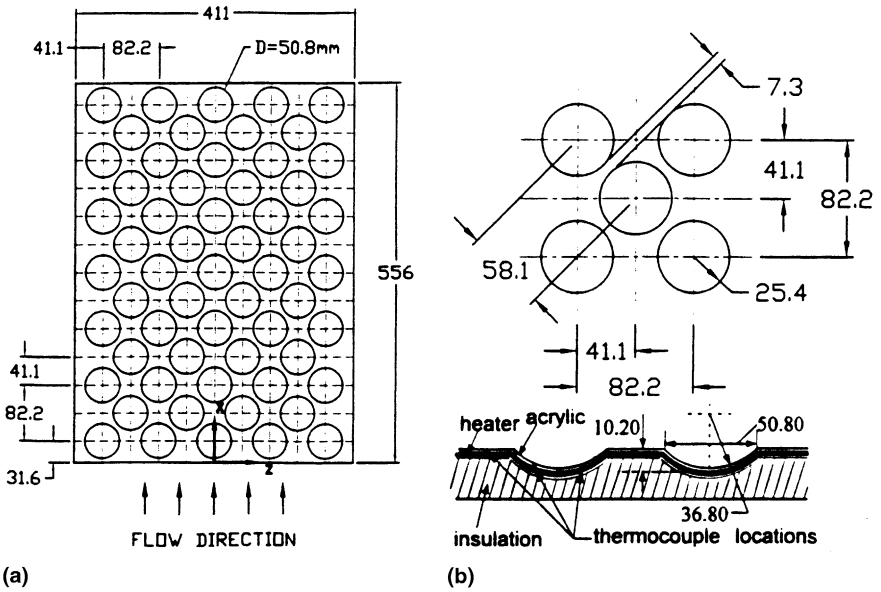

Fig. 2. Schematic diagrams of: (a) the entire dimpled test surface; (b) individual dimple geometry details. All dimensions are given in mm.

provided by the etched-foil heater is divided by the total area of the test surface (flat portions and dimples). Thus, local heat transfer coefficients and local Nusselt numbers are based on the same area. This is a different approach than employed by Chyu et al. [8] and Moon et al. [10], where heat transfer coefficients, determined using transient liquid crystal techniques, are based on heat flux levels which are based on flat projected area. As a result, heat transfer coefficients from those studies are about 16.4% higher than values from the present study when compared for the same geometry and flow conditions.

Spatially-resolved temperature distributions along the dimpled test surface are determined using infrared imaging in conjunction with thermocouples, energy balances, digital image processing, and *in situ* calibration procedures. To accomplish this, the infrared radiation emitted by the heated interior surface of the channel is captured using a Video Therm 340 Infrared Imaging Camera, which operates at infrared wavelengths from 8 to 14 μm. Temperatures, measured using the calibrated, copper–constantan thermocouples distributed along the test surface adjacent to the flow, are used to perform the *in situ* calibrations simultaneously as the radiation contours from surface temperature variations recorded.

This is accomplished as the camera views the test surface through a custom-made, zinc–selenide window (which transmits infrared wavelengths between 6 and 17 μm) located on the top wall of the test section. Reflection and radiation from surrounding laboratory sources are minimized using an opaque shield which covers the camera lens and the zinc–selenide window. Frost build-up on the outside of the window is eliminated using a small heated air stream. The window is located just above the tenth and twelfth rows of dimples downstream from the leading edge of the test surface. Five to six thermocouple junction locations are usually present in the infrared field viewed by the camera. The exact spatial locations and pixel locations of these thermocouple junctions and the coordinates of a 12.7 cm × 12.7 cm field of view are known from calibration maps obtained prior to measurements. During this procedure, the camera is focused, and rigidly mounted and oriented relative to the test surface in the same way as when radiation contours are recorded.

With these data, gray scale values at pixel locations within video taped images from the infrared imaging camera are readily converted to temperatures. Because such calibration data depend strongly on camera adjustment, the same brightness, contrast, and aperture camera settings are used to obtain the experimental data. The *in situ* calibration approach rigorously and accurately accounts for these variations.

Images from the infrared camera are recorded as 8-bit gray scale images on commercial videotape using a Panasonic AG-1960 video recorder. Images are then digitized using NIH Image v1.60 software, operated on a Power Macintosh 7500 PC computer. Subsequent software is used to convert each of 256 possible gray scale values to temperature at each pixel location using calibration data, and then determines values of local Nusselt numbers. Thermal conductivity in the Nusselt number is based on the average of the local wall tem-

perature and the temperature of air at the upstream inlet. Contour plots of local surface temperature and Nusselt number are prepared using DeltaGraph v4.0 software. Each individual image covers a 300 pixel × 300 pixel area. Sargent et al. [11], and Hedlund and Ligrani [12] provide additional details on the infrared imaging and measurement procedures.

2.3. Flow visualization

Flow visualization using smoke is used to identify vortex structures and other secondary flow features. Smoke from two or three horizontally oriented smoke wires is employed for this purpose. These are located 3.2, 6.4, and 19.1 mm from the surface over the fifth row of dimples at $x = 200$–210 mm. To accomplish this, each wire is first coated with Barts Pneumatics super fluid and then powered using a Hewlett Packard 6433B DC power supply. With this arrangement, the smoke forms into single thin lines parallel to the test surface. As the smoke is advected downstream, the secondary flows which accompany vortex and secondary flow development cause the smoke to be rearranged in patterns which show the locations and distributions of these flow phenomena. Smoke patterns are illuminated in different planes using thin sheets of light provided by a Colotran ellipsoidal No. 550, 1000 W spot light, and light slits machined in two parallel metal plates. Images are recorded using a Dage-MTI CCD72 camera and control box with a Computer 12.5 mm, F1.8 lens, connected to a Panasonic AG-1960 type 4-head, multiplex video cassette recorder. Images recorded on video tape (taken individually or in sequence) are then digitized using a Sony DCR-TRV900 digital video camera recorder. The resulting images are then further processed using a Power Macintosh 7500 PC computer, and finally printed using a Panasonic PV-PD 2000 digital photo printer. Additional discussion of the procedures used for flow visualization is provided by Ligrani [13].

2.4. Uncertainty estimates

Uncertainty estimates are based on 95% confidence levels, and determined using procedures described by Kline and McClintock [14] and Moffat [15]. Uncertainty of temperatures measured with thermocouples is pluemn ±0.15 °C. Spatial and temperature resolutions achieved with the infrared imaging are about 0.52 mm and 0.8 °C, respectively. This magnitude of temperature resolution is due to uncertainty in determining the exact locations of thermocouples with respect to pixel values used for the *in situ* calibrations. Local Nusselt number uncertainty is then about ±6.8% for $T_{oi}/T_w = 0.68$. Corresponding Nusselt number ratio uncertainty is about ±0.19 (for a ratio of 2.00) or ±9.6%. Local Nusselt number uncertainties then increase as T_{oi}/T_w becomes larger to reach maximum values of about ±9.6% for $T_{oi}/T_w = 0.92$–0.94 Note that all uncertainties of local Nusselt numbers consider variations of surface heat flux which may be present due to small changes of the thickness of the acrylic which comprises the dimpled test surface. Reynolds number uncertainty is about ±1.7% for Re_H of 10 200.

3. Experimental results and discussion

3.1. Baseline Nusselt numbers

Baseline Nusselt numbers are measured with a smooth test surface replacing the dimpled test surface at the same Reynolds numbers as employed in the dimpled channel. Other than the test surface, all geometric characteristics of the channel are the same as when a dimpled test surface is installed. These baseline values are used to normalize dimpled test surface values, and are thus used as a basis of comparison to dimpled test surface values. All baseline measurements are made with thermally and hydraulically fully developed channel flow, at a ratio of inlet stagnation temperature to wall temperature of 0.93–0.94.

Note that channel height H is measured from the top wall to the flat portions of the bottom wall (or to the dimple horizon) between the dimples. The ratios of channel height to dimple print diameter H/D which are employed in the study, are 0.20, 0.25, 0.50, and 1.00. To obtain these ratios with channel height measured to the bottom of the dimples, 0.20 is added to each value of H/D.

3.2. Local Nusselt number variations with Z/D at different H/D

Fig. 3 shows the locations where the data in Figs. 4 and 5 and Figs. 7–10 are obtained. Figs. 4 and 5 give local Nusselt numbers measured on the dimpled test surface as dependent upon Z/D at constant X/D of 9.35 and 8.50, respectively. Figs. 7 and 8 then give local Nusselt numbers as dependent upon X/D at constant Z/D of 0.0 and 0.45, respectively. Reynolds number Re_H is about constant for these data, as it ranges from 9 800 to 10 300. T_{oi}/T_w is also constant, ranging from 0.92 to 0.94.

The lines along the dimpled surface where these measurements are made are shown in Fig. 3. Shown are dimples in the tenth and thirteenth rows from the beginning of the test surface. According to Fig. 3, a line through $X/D = 9.35$ is located in the upstream part of dimple cavities in the 12th row (at Z/D from −1.2 to −0.5 and at Z/D from +0.5 to +1.2), and just downstream of a dimple in the 11th row at Z/D from −0.5 to

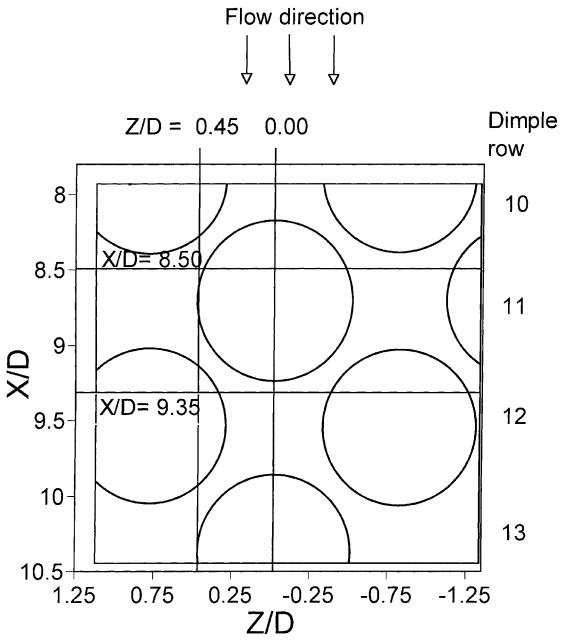

Fig. 3. Schematic of a portion of the dimpled test surface showing the X/D and Z/D surface locations of the local measurements given in Figs. 4–5 and Figs. 7–10.

+0.5. Fig. 3 additionally shows that a line through $X/D = 8.50$ is located just downstream of dimples in the 10th row (at Z/D from −1.2 to −0.5, and at Z/D from

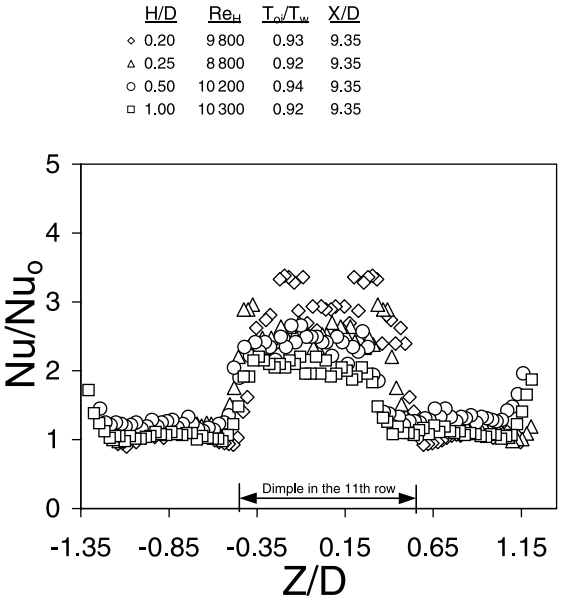

Fig. 4. Local Nu/Nu_0 as dependent upon Z/D, measured at different H/D at the twelfth row of dimples along a line of constant X/D of 9.35.

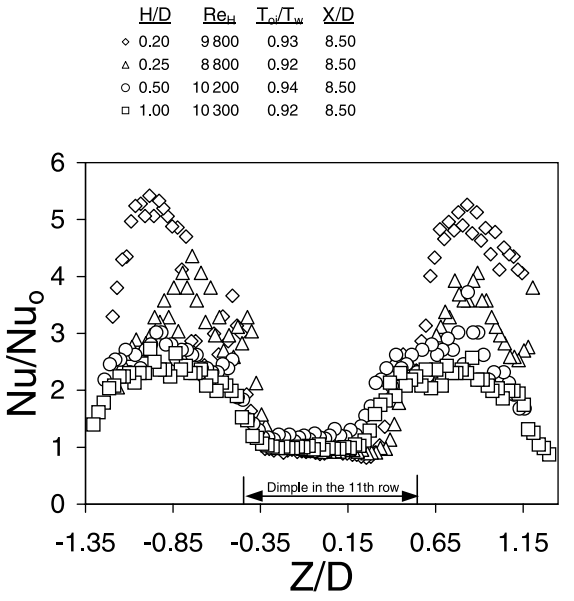

Fig. 5. Local Nu/Nu_0 as dependent upon Z/D, measured at different H/D at the eleventh row of dimples along a line of constant X/D of 8.50. Symbols defined in Fig. 4.

+0.5 to +1.2), and through the upstream portion of dimple cavities in the 11th row (at Z/D from −0.5 to +0.5).

Notice that the regions with the highest local Nu/Nu_0 values are present over different Z/D ranges in Figs. 4 and 5. However, in both cases, these high Nu/Nu_0 regions are located just downstream of dimple cavities. Regions with lower local Nu/Nu_0 are then measured within dimple cavities. Here, local Nu/Nu_0 values are in the vicinity of 1.0, and Nu/Nu_0 values change only slightly at each Z/D value as H/D is varied. In contrast, local Nu/Nu_0 values continually increase as H/D decreases on the flat surface regions downstream of the dimples. Here, local Nusselt numbers are also augmented considerably relative to a channel with smooth walls ($Nu/Nu_0 = 1.0$).

Another interesting feature of the data in Fig. 4 are two distinct peaks in the local Nu/Nu_0 distributions as Z/D varies. These are located just downstream a dimple located in row 11, and are most apparent for $H/D = 0.20,\ 0.25$, $X/D = 9.35$, and at Z/D from −0.5 to +0.5 in Fig. 4. These peaks are due to the vortex pairs and vortical fluid shed from the spanwise edges and diagonal edges of dimples.

3.3. Instantaneous flow structure from flow visualizations at different H/D

Such vortical events are evident in the flow visualization images presented in Figs. 6(a)–(c) for H/D of 0.25, 0.50, and 1.0, respectively. In each case, a time

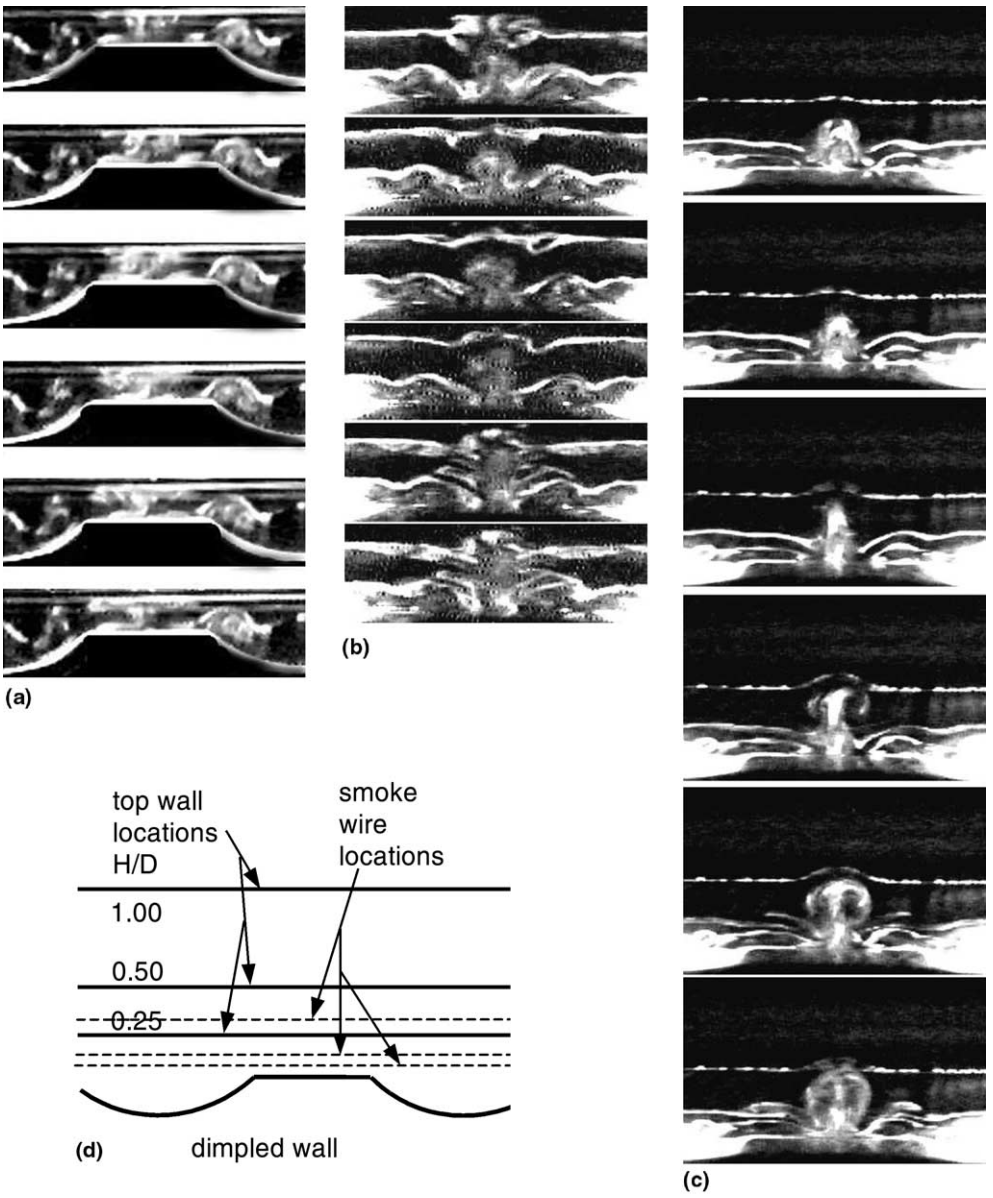

Fig. 6. Time-sequences of flow visualization images in the spanwise–normal light plane at $X/D = 8.0$ just downstream of a dimple in the ninth row. Time interval between adjacent images is 1/30 s. (a) $Re_H = 610$ and $H/D = 0.25$; (b) $Re_H = 900$ and $H/D = 0.5$; (c) $Re_H = 2560$ and $H/D = 1.0$; (d) layout of visualized flow cross-sectional plane.

sequence of instantaneous flow visualization images is presented for the spanwise–normal plane positioned at $X/D = 8.0$. Fig. 3 shows that this location is one or two rows of dimples upstream of the locations where the heat transfer data presented in Figs. 4 and 5 are measured. Each image in Figs. 6(a)–(c) shows a smoke pattern resulting from the vortical structures just above the flat surface which is located just downstream of a dimple cavity in the ninth row. The same features are also present just downstream of the eleventh row of dimples at $X/D = 9.35$, where the Nu/Nu_0 data given in Fig. 4 are measured. Each view in Figs. 6(a)–(c) is obtained over the entire width of the channel, and the spanwise extent of each image approximately covers one complete period of dimple geometry. Flow is out of the plane of the paper, and dimples are located at the bottom edge of each image. Each "mushroom-shaped" smoke pattern in Figs. 6(a)–(c) indicates the presence of a pair of counter-rotating vortices. Fig. 6(d) shows the layout of the spanwise–

normal plane in which the flow is illuminated and visualized.

Regardless of the value of H/D, Figs. 6(a)–(c) show that each dimple located on the bottom surface periodically sheds about three vortex pairs along with other vortical fluid. These are generally apparent in the central portion of each image. A distinct upwash region is located between the two vortices in each par. The most prominent of these vortex pairs and upwash regions is located centrally relative to a dimple center. It is often roughly symmetric with respect to a centerline/normal plane, and the associated upwash region is in the streamwise–normal plane also located approximately along the centerline of each dimple. The other two vortex pairs and associated upwash regions are located near the left and right spanwise edges of each dimple, often near diagonal dimple locations, or just downstream of these locations. These vortex pairs, which form near dimple diagonals, are often in the form of collections of vortex pairs, or sometimes, short "braids" vortical fluid [1].

All of these vortex pairs are stretched as they are advected downstream (by the streamwise bulk flow above the dimple horizon), which causes them to become smaller in cross-section, more elongated, and more distorted. As this happens, the tubes of vorticity periodically impact on the downstream rim of a dimpled edge and on the flat surface just downstream of this dimple, and then advect just above and into the dimple volumes which are located diagonal and adjacent to the originating dimple. As a result, local Nusselt number augmentations are especially pronounced near the downstream rims of dimples as well as on flat surfaces downstream of and between dimples.

The periodicity of vortex shedding events is evident in each time-sequence shown in Figs. 6(a)–(c) for all three H/D values. The periodicity is more apparent as H/D increases, and takes the form of a repeated cycle of events, where each cycle consists of inrush of fluid to each dimple, followed by outflow and vortex shedding. The outflow part of the cycle is then when the most prominent vortical structures form. In many cases, the periodicity of the vortex pairs near the dimple diagonals is out-of-phase with the periodicity of the central upwash region and associated vortex pair.

Also indicated in Figs. 6(a)–(c) are the increases in the strengths of the secondary flows associated with vortical motions as H/D decreases. This is evidenced by greater wrapping and secondary arrangement of smoke patterns and trajectories. The data in Figs. 6(a)–(c) are for Re_H of 610, 900, and 2560 for H/D of 0.25, 0.50, and 1.0, respectively. These Re_H values are selected because they all give about the same streamwise bulk velocity averaged over the channel cross-section. The phenomena shown in Figs. 6(a)–(c) are also expected to be present at the higher Reynolds numbers employed for the surface heat transfer data. Thus, the increases in vortex strength, evidenced by the data in Figs. 6(a)–(c), produce greater *local* heat transfer augmentations in Figs. 4, 5, 7, and 8.

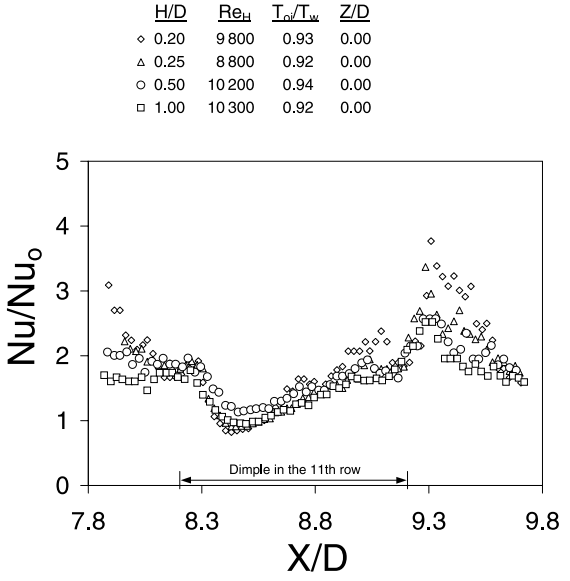

Fig. 7. Local Nu/Nu_0 as dependent upon X/D, measured at different H/D at the eleventh row of dimples along a line of constant Z/D of 0.00. Symbols defined in Fig. 4.

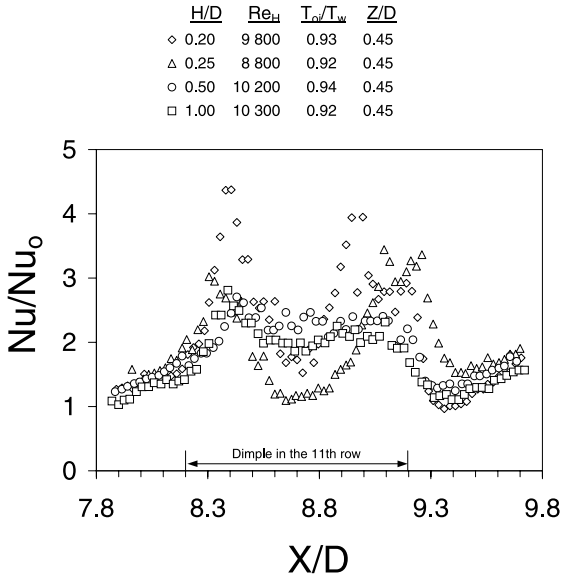

Fig. 8. Local Nu/Nu_0 as dependent upon X/D, measured at different H/D at the eleventh row of dimples along a line of constant Z/D of 0.45. Symbols defined in Fig. 4.

3.4. Local Nusselt number variations with X/D at different H/D

Figs. 7 and 8 give local Nusselt numbers as dependent upon X/D at constant Z/D of 0.00 and 0.45, respectively, as mentioned. The overall geometric arrangement, Reynolds numbers Re_H, and temperature ratios T_{oi}/T_w are the same as for Figs. 4 and 5. The lines along the dimpled surface where these measurements are made are shown in Fig. 3. Note that $Z/D = 0.00$ corresponds to the spanwise center of the test section, and that $Z/D = 0.45$ is positioned along the spanwise edges of dimples.

The $Z/D = 0.0$ data in Fig. 7 are then located along a line through the spanwise centerline of the central dimple in the eleventh row. Notice that Nu/Nu_0 magnitudes for all H/D values are in the victinity of 2.0 at $7.9 < X/D < 8.2$, just upstream of the dimple. Values then decrease as X/D increases through the upstream portion of the dimple cavity, with the lowest Nu/Nu_0 magnitudes located at X/D from 8.4 to 8.7, just upstream of the center of the dimple. Here Nu/Nu_0 values increase somewhat as H/D decreases. This trend is even more apparent at larger X/D from 9.0 to 9.7, where significant Nu/Nu_0 augmentations are present due to: (i) reattachment of the shear layer that forms across the top of each dimple, and (ii) increased turbulence transport resulting from vortical fluid and vortical structures shed from each dimple and then advected over the flat surface just downstream(Figs. 6(a)–(c)).

Local Nu/Nu_0 data in Fig. 8 for $Z/D = 0.45$ increase as H/D decreases at many X/D locations. These variations are due to the vortical fluid and vortex pairs which form and develop near the spanwise edges of the dimples and along dimple diagonals. As mentioned earlier, these sometimes take the form of braids of vortical fluid, and often produce flow interactions between neighboring dimples in diagonal directions. The Nu/Nu_0 increase with decreasing H/D in Fig. 8 indicate that the local turbulent transport capabilities of the vortices and braids of vortical fluid generally increase as H/D decreases. The largest increases with diminishing H/D are located near diagonals of dimples in the tenth and eleventh rows (also see Figs. 3, 4 and 5). These vortical fluid motions, and the mixing associated with them, likely also produce enhanced heat transfer coefficients on the smooth wall (opposite to the dimpled surface).

3.5. Local Nusselt number variations with X/D and Z/D at different T_{oi}/T_w

Figs. 9 and 10 give local Nusselt number ratios as dependent upon Z/D at constant $X/D = 9.35$, and as dependent upon X/D at constant $Z/D = 0.00$, respectively. These data are presented to show the effects of temperature ratio T_{oi}/T_w, as Reynolds number Re_H and H/D are both held approximately constant at 8800–11 100, and 0.25, respectively. The lines along the dimpled surface where these measurements are made again as shown in Fig. 3.

From the results in Figs. 9 and 10, it is evident that local Nu/Nu_0 values increase as T_{oi}/T_w decreases at most

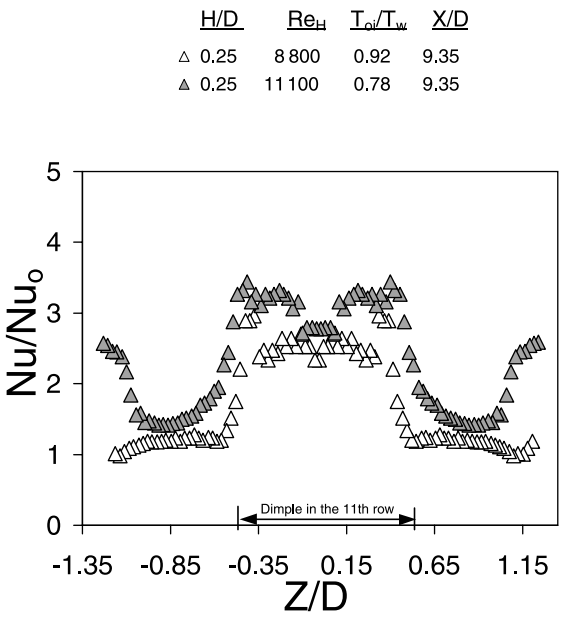

Fig. 9. Local Nu/Nu_0 as dependent upon Z/D, measured at $H/D = 0.25$ at different T_{oi}/T_w at twelfth row of dimples along a line of constant X/D of 9.35. Symbols defined in Fig. 10.

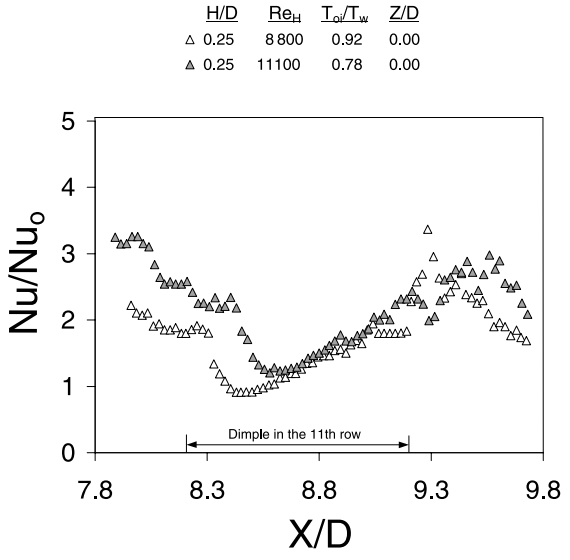

Fig. 10. Local Nu/Nu_0 as dependent upon X/D, measured at $H/D = 0.25$ and different T_{oi}/T_w at the eleventh row of dimples along a line of constant Z/D of 0.00.

of X/D and Z/D values examined. The increases are especially apparent on the flat surfaces just downstream of dimples and in the upstream parts of dimple cavities. These changes occur because vortex pairs and vortical fluid advect larger amounts of colder fluid from the central parts of the channel to regions near the heated dimpled surface as the temperature ratio T_{oi}/T_w decreases. Local Nu/Nu_0 variations with T_{oi}/T_w are then much smaller within the central and downstream parts of dimple cavities.

4. Summary and conclusions

Experimental results, measured on and above a dimpled test surface placed on one wall of a channel, are given for Reynolds numbers (Re_H) from about 600 to about 11 000 and ratios of air inlet stagnation temperature to surface temperature (T_{oi}/T_w) ranging from 0.78 to 0.94. These include flow visualizations, and spatially resolved local Nusselt numbers. Ratios of channel height to dimple print diameter of 0.20, 0.25, 0.50, and 1.00 are employed. The ratio of dimple depth to dimple print diameter is 0.2.

Visualized flow smoke patterns show that the vortex pairs, which are periodically shed from the dimples, become stronger as non-dimensional channel height H/D decreases. These increases in strength are evidenced by smoke patterns with greater wrapping and secondary arrangement of smoke trajectories. These phenomena lead to local Nusselt number augmentations which are especially pronounced near the downstream rim of each dimple, and along two strips of flat surface located near the spanwise edges of downstream-diagonal, adjoining dimples. The effects of these vortex induced secondary flows on heat transfer augmentations is then illustrated by the increases of local Nusselt number values over these same locations (with respect to the dimples) as H/D decreases.

Local Nusselt number augmentations also develop as the vortex pairs and vortical fluid advect colder fluid from the central parts of channel to regions near the heated dimple surface. This occurs in larger and larger doses as T_{oi}/T_w, the ratio of inlet stagnation temperature to local surface temperature, decreases. Such behavior is evidenced by local Nusselt number ratios, which increase substantially as T_{oi}/T_w decreases (regardless of the magnitude of H/D) because of buoyancy and variable property influences.

Acknowledgements

The work presented in this paper was performed as a part of the Advanced Turbine System Technology Development Project, sponsored both by the US Department of Energy and Solar Turbines. Dr. Hee-Koo Moon and Dr. Boris Glezer are acknowledged for useful discussions of the results. Mike Hill and Mounir Sabbagh helped in acquiring some of the data presented.

References

[1] G.I. Mahmood, M.L. Hill, D.L. Nelson, P.M. Ligrani, H.-K. Moon, B. Glezer, ASME Trans. Turbomachinery 123 (2001) 115.
[2] V.N. Afanasyev, Y.P. Chudnovsky, A.I. Leontiev, P.S. Roganov, Exp. Thermal Fluid Sci. 7 (1993) 1.
[3] M.Y. Blen'kiy, M.A. Gotovskiy, B.M. Lekakh, B.S. Fokin, K.S. Dolgushin, Heat Transfer Res. 25 (1994) 196.
[4] V.S. Kesarev, A.P. Kozlov, Heat Transfer Res. 25 (1994) 156.
[5] V.I. Terekhov, S.V. Kalinina, Y.M. Mshvidobadze, Russ. J. Eng. Thermophys. 5 (1995) 11.
[6] A.V. Schukin, A.P. Koslov, R.S. Agachev, ASME Paper No. 95-GT-59 ASME 40th International Gas Turbine and Aeroengine Congress and Exposition, Houston, TX, 1995.
[7] Y.F. Gortyshov, I.A. Popov, R.D. Amirkhanov, K.E. Gulitsky, Proceedings of 11th International Heat Transfer Congress 6 (1998) 83.
[8] M.K. Chyu, Y. Yu, H. Ding, J.P. Downs, F.O. Soechting, ASME Paper No. 97-GT-437 ASME 42nd International Gas Turbine and Aeroengine Congress and Exposition, Orlando, FL, 1997.
[9] Y.-L. Lin, T.I.-P. Shih, M.K. Chyu, ASME Paper No. 99-GT-263 ASME 44th International Gas Turbine and Aeroengine Congress and Exposition, Indianapolis, IN, 1999.
[10] H.-K. Moon, T. O'Connell, B. Glezer, ASME Paper No. 99-GT-163 ASME 44th International Gas Turbine and Aeroengine Congress and Exposition, Indianapolis, IN, 1999.
[11] S.R. Sargent, C.R. Hedlund, P.M. Ligrani, Meas. Sci. Technol. 9 (1998) 1974.
[12] C.R. Hedlund, P.M. Ligrani, ASME Trans. J. Turbomachinery 122 (2000) 375.
[13] P.M. Ligrani, Meas. Sci. Technol. 11 (2000) 992.
[14] S.J. Kline, F.A. McClintock, Mech. Eng. 75 (1953) 3.
[15] R.J. Moffat, Exp. Thermal Fluid Sci. 1 (1998) 3.